Materials Characterization 229 (2025) 115587

Contents lists available at ScienceDirect

Materials Characterization

journal homepage: www.elsevier.com/locate/matchar

Effects of heat treatment on microstructure, mechanical properties and irradiation response of LPBF GH3535 superalloy

Zhangjie Sun [a], Feida Chen [a,*], Jianjian Li [c,*], Kun Yang [a], Xiaobin Tang [a,b,*]

[a] Department of Nuclear Science and Technology, Nanjing University of Aeronautics and Astronautics, Nanjing 211106, China
[b] Key Laboratory of Nuclear Technology Application and Radiation Protection in Aerospace, Ministry of Industry and Information Technology, Nanjing 211106, China
[c] Shanghai Institute of Applied Physics, Chinese Academy of Science, Shanghai 201800, China

ARTICLE INFO

Keywords:
Laser powder bed fusion
GH3535 superalloy
Tensile property
Helium bubble

ABSTRACT

Additive manufacturing (AM) offers a promising approach for the structural optimization of components in next generation advanced reactors. However, AM alloys often struggle to achieve a balanced combination of the mechanical properties and irradiation resistance. In this study, a novel GH3535 superalloy with a theoretical density of 99.996 % was fabricated using laser powder bed fusion (LPBF), followed by a two-step heat treatment consisting of hot isostatic pressing (HIP) and solid solution heat treatment (SSHT). The properties of three types of LPBF GH3535 samples were compared to assess the influence of heat treatment on their microstructure and mechanical properties. Tensile testing revealed that the LPBF-HIP-SSHT sample exhibited superior ductility compared to the LPBF sample, both at room temperature and 700 °C. Nanoindentation tests were conducted to evaluate the irradiation hardening behavior of the alloys. TEM analysis and helium bubble statistical evaluation showed that the LPBF and LPBF-HIP-SSHT samples had similar helium bubble sizes and number densities. When compared to the LPBF-HIP sample, the LPBF-HIP-SSHT GH3535 alloy demonstrated superior helium tolerance and enhanced resistance to irradiation hardening, largely attributed to the presence of a significant amount of nano-carbides. This study offers important insights into the design and optimization of LPBF GH3535 for nuclear industry applications.

1. Introduction

The rapid development of clean energy sources, such as nuclear power, is expected to address the growing issue of energy shortages [1,2]. The advancement of new fourth-generation reactor technologies will further improve the safety and efficiency of nuclear energy [3]. Additive manufacturing (AM), which offers significant advantages in the efficient production of complex components, holds great potential and value in the design and fabrication of precise structural parts for next-generation reactors [4–6]. Superalloys are currently among the most valuable key materials for AM [7–9]. Focusing on molten salt reactors (MSRs), one of the six types of fourth-generation reactors [10,11], GH3535 alloy is a primary candidate material for internal components and fuel assemblies [12–14]. GH3535 is a solid-solution-strengthened alloy known for its excellent corrosion resistance to molten salts, superior radiation resistance, and outstanding high-temperature strength [15,16]. The specific elemental composition design, including an appropriate amount of Mo, enhances the alloy's high-temperature creep resistance, while 7 wt% Cr content improves oxidation resistance without compromising corrosion resistance. However, the complex composition of the current high-performance GH3535 alloy does not align well with the non-equilibrium and highly constrained AM process, leading to issues such as cracking and performance discrepancies, which hinder its engineering applications [17–19]. Given that it operates in a high-neutron-irradiation environment, the irradiation resistance of additively manufactured GH3535 is a critical consideration. Therefore, the development of high-performance AM GH3535 alloys has become a bottleneck restricting material selection for molten salt reactor equipment.

The GH3535 alloy (UNS N10003 alloy), a Ni-Mo-Cr-based superalloy [20], may develop pores during AM due to incomplete powder melting and may form secondary phases distinct from traditional melted (TM) GH3535 due to repeated melting. Furthermore, due to the nature of AM, a high density of sub-grain boundaries may form [21]. These unique microstructures can lead to deviations in the performance of AM GH3535 compared to TM GH3535 [22]. Specifically, pores may degrade

* Corresponding authors.
E-mail addresses: fdchen@nuaa.edu.cn (F. Chen), lijianjian@sinap.ac.cn (J. Li), tangxiaobin@nuaa.edu.cn (X. Tang).

https://doi.org/10.1016/j.matchar.2025.115587
Received 9 December 2024; Received in revised form 20 September 2025; Accepted 22 September 2025
Available online 27 September 2025

the mechanical properties, while sub-grain boundaries may enhance irradiation resistance [23–25]. Hot isostatic pressing (HIP) and solid-solution heat treatment (SSHT) are effective methods for eliminating these unique microstructures [26–28]. The TM GH3535 alloy is highly sensitive to heat treatment processes, suggesting that combining AM with HIP and SSHT could lead to the development of GH3535 alloys that meet the performance requirements of molten salt reactors.

Laser powder bed fusion (LPBF) is a metal AM printing technology based on high-energy laser beams [29]. In this study, LPBF was employed to develop a novel GH3535 alloy. Two-step heat treatments—Hot HIP and SSHT—were subsequently applied to prepare the LPBF-HIP GH3535 and LPBF-HIP-SSHT GH3535 samples. The microstructure and mechanical properties of the LPBF samples were evaluated at room temperature (RT) and 700 °C, both before and after heat treatment, using cast Ni-Mo-Cr-based alloys (CA) as reference materials. He^{2+} ion irradiation experiments were conducted at fluences of 5×10^{16} ions/cm^2 and 5×10^{17} ions/cm^2 at 700 °C. Microstructural changes, such as the formation of helium bubbles and secondary phases, were analyzed via transmission electron microscopy (TEM). Nanoindentation tests were performed to assess irradiation-induced hardening behavior. The influence of the two-step heat treatment on the formation and evolution of irradiation-induced helium bubbles was also examined.

2. Experimental

2.1. Material and power preparation

The CA alloy used in this study was supplied by the manufacturer in the form of a melted block with dimensions of 100 × 100 × 100 mm^3. Vacuum induction melting gas atomization (VIGA) is an effective method for the industrial-scale production of non-active metal powders [30], which was employed to prepare GH3535 powder. The powder, sieved through 270–800 mesh, was used for subsequent sample printing. The optimize the particle size distribution for LPBF requirements, the powder underwent a ball-milling process. Four stainless steel jars, each containing 100 g of powder, were used with stainless steel balls at a ball-to-powder ratio (BPR) of 5:3 for 4 h. Prior to milling, the jars were evacuated to a pressure of 10^{-2} Pa and backfilled with an argon atmosphere. SEM-EDS analysis of both the powder and the final products confirmed the absence of oxygen, demonstrating effective prevention of oxidation during the entire milling process. According to ISO/ASTM standards, the orifice diameter of the Hall flow meter (BT-1001) is 5.0 mm, with a powder quantity of 50 g. After drying at 60 °C for 4 h, the measured Hall flowability (14.5 s/50 g) was considered suitable for the LPBF process. The particle size analysis revealed the following percentile diameters: d10 = 12.9 μm, d50 = 29.6 μm, and d90 = 54.9 μm.

2.2. Selective laser melting process

The LPBF GH3535 cuboid-shaped samples, with dimensions of 10 × 10 × 2 mm^3, were fabricated using an LPBF machine (SLM125, Solutions, Germany) with a maximum output power of 400 W in an argon atmosphere. The optimized printing parameters are provided in Table 1.

The chemical compositions of CA Ni-Mo-Cr and LPBF GH3535, as determined by energy-dispersive X-ray fluorescence (EDXRF), are presented in Table 2.

Table 1
Printing parameters of LPBF GH3535 superalloy.

Atmosphere	Power (W)	Scanning rate (mm/s)	Line spacing (mm)	Spot diameter (μm)
Ar	300	1000	0.05	70

Table 2
Chemical compositions (wt%) of the CA Ni-Mo-Cr and LPBF GH3535.

	Ni	Cr	Mn	Fe	Mo	Ti
CA Ni-Mo-Cr	Bal.	7.11	0.36	4.26	15.41	0
LPBF GH3535	Bal.	7.10	0.33	4.74	15.32	0.02

2.3. Post processing

The HIP process was carried out in a Mo-furnace of a Quintus QIH 9 hot-isostatic press at 1050 °C for 3 h under an Ar atmosphere at a pressure of 1000 MPa. Subsequently, the HIP GH3535 samples and CA Ni-Mo-Cr samples underwent further solid solution heat treatment (SSHT) in an air atmosphere at 1177 °C, with a heating rate of 10 °C/min, for 20 or 60 min, followed by water quenching.

2.4. Mechanical performance experiment

Charpy impact specimens of the CA Ni-Mo-Cr and LPBF GH3535 samples were prepared using wire-cut Electrical Discharge Machining (WEDM) and LPBF, respectively, with dimensions of 55 × 10 × 10 mm^3. Impact testing was performed on both the CA Ni-Mo-Cr and LPBF GH3535 samples at RT and 200 °C using an impact testing machine (RPK450, Zwick, Germany). Compared to the CA Ni-Mo-Cr samples, which were tested before and after heat treatment, LPBF GH3535 samples in three different states were prepared as bone samples for tensile testing at RT and 700 °C, with a tensile rate of 3.5 mm/min. A schematic diagram showing the bone sample size is provided in Fig. S1. Nanoindentation tests were performed on both pre- and post-irradiation samples using a G200 Nano Indenter to obtain indentation depth and hardness curves. A Berkovich-type diamond indenter and continuous stiffness measurement (CSM) method were utilized. The maximum indentation depth was fixed at 3 μm to cover the entire irradiated region. To ensure statistical reliability, more than 20 indentations were conducted for each sample, and the hardness data were averaged.

2.5. Irradiation experiment

The CA Ni-Mo-Cr, LPBF GH3535, LPBF-HIP GH3535, and LPBF-HIP-SSHT GH3535 specimens were irradiated with 540 keV He^{2+} ions at fluences of 5×10^{16} and 5×10^{17} ions/cm^2 at 700 °C. The corresponding displacements per atom (dpa) and He concentration as a function of depth were predicted using the SRIM-2013 program in the "Kinchin-Pease quick calculation" mode, as shown in Fig. 1.

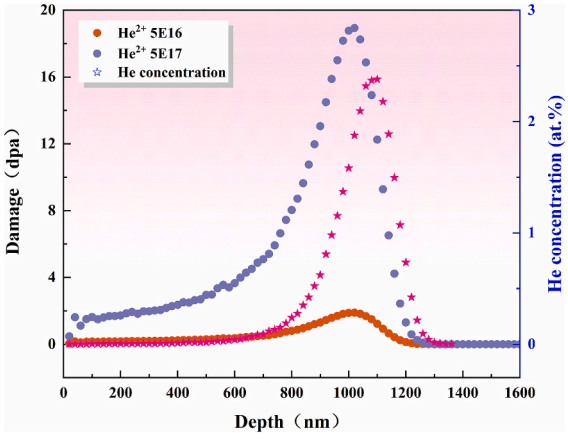

Fig. 1. SRIM calculation results of irradiation damage dose and He concentration as a function of depth for LPBF GH3535 superalloy.

2.6. . Microscopic characterization

The samples were ground with 2000 mesh sandpaper and subsequently polished to a mirror finish. The relative densities of all printed samples were measured using industrial computed tomography (CT). CT images of the core samples revealed the presence of pores, their sizes, and the connectivity between them. As shown in Fig. S2, points marked in different colors correspond to the locations of the holes or defects, and the software was used to calculate the total volume of these holes. The defect densities for particles larger than 30 μm in the samples treated with LPBF, LPBF-HIP, and LPBF-HIP-SSHT were 0.004 %, 0.027 %, and 0.043 %, respectively, indicating that the density of all samples exceeds 99.9 %. Phase identification of all samples was performed using an X-ray diffractometer (PAN alytical, Holland) within a diffraction range of 20° to 100° at a scanning speed of 10°/min. The surface microscopy of the samples was examined using metallographic microscopy (Scope.A1, Zeiss) and scanning electron microscopy (TESCAN LYRA3 GM). Thin foils for TEM analysis were prepared using the focused ion beam (FIB) lift-out technique on an FEI Helios G4 workstation. The microstructures of both the pristine and ion-irradiated samples were analyzed using TEM (Spectra 300, operated at 300 kV) in bright field (BF) and high-angle annular dark field scanning transmission electron microscopy (HAADF-STEM) imaging modes.

3. Results

3.1. Microstructure

3.1.1. XRD

Figs. 2 (a) and (b) present the XRD patterns of CA Ni-Mo-Cr and LPBF GH3535 before and after heat treatment, respectively. As shown in Figs. 2(a), the γ phase is the primary phase, and no primary observed in the pristine CA Ni-Mo-Cr, GH3535 powder, or LPBF GH3535 prior to heat treatment. Compared to the CA Ni-Mo-Cr sample, the diffraction peaks of LPBF GH3535 are broader. The XRD patterns of the samples after heat treatment are shown in Fig. 2 (b), where secondary phase diffraction peaks are observed in all CA, LPBF-HIP, and LPBF-HIP-SSHT samples. After heat treatment, the 2θ angles of the γ diffraction peaks for all samples were recorded and summarized in Table 3. As the heat-treatment duration was extended from 20 to 60 min, a notable right shift in the diffraction peaks of CA Ni-Mo-Cr and LPBF GH3535 was observed.

As shown in Fig. 2, the strongest peak for both the CA sample and GH3535 powder is γ-111. This occurs because both the CA sample and GH3535 powder tend to form equiaxed grains, and the (111) planes naturally dominate due to their low surface energy. The strongest peak of LPBF GH3535 is γ-220, which results from preferential grain growth along the build direction, consistent with the reported epitaxial growth observed in AM alloys. The heat treatment process, including HIP and solid solution treatment, may alter the initial texture, causing the strongest peak of the HIP and SSHT samples to shift to γ-200 [31].

Table 3
Diffraction peaks of γ-Ni with 2θ of five main peaks.

Samples	111	200	220	311	222
CA-20	43.316.	50.499	74.494	90.566	95.926
CA-60	43.362	50.571	74.580	90.638	95.959
LPBF-HIP	43.428	50.610	74.619	90.700	96.022
LPBF-HIP-SSHT-20	43.343	50.545	74.520	90.595	95.959
LPBF-HIP-SSHT-60	43.389	50.600	74.576	90.641	/

In X-ray diffraction analysis, peak broadening can be attributed to several factors including grain size, lattice strain, and defect density. As previously mentioned, the broader diffraction peaks suggest that the LPBF samples likely possess different grain sizes compared to the CA samples. Further investigation of grain size evolution will be presented in the next section. The high-temperature heat treatment led to the precipitation of additional carbide phases in the matrix, which were identified as M_6C precipitates [32]. The precipitation of these carbides increased with longer heat treatment durations, along with an enhanced precipitation of alloying elements from the matrix, resulting in a reduction in lattice spacing.

3.1.2. Grain structure

Metallographic micrographs of the GH3535 microstructure before and after heat treatment are shown in Fig. 3. Fig. 3 (a) illustrates that the original CA Ni-Mo-Cr sample exhibits a coarse-grained structure with considerable grain size variation, with an average grain size of 84.75 μm, ranging from 63 to 110 μm. As depicted in Fig. 3 (f), secondary phases show localized aggregation with sizes around 5 μm. After 60 min of heat treatment, Fig. 3 (b) and (g) reveal that the grains in the CA Ni-Mo-Cr sample form a more uniform equiaxed structure, with an average grain size of 99.13 μm. The carbides in the CA samples are distributed along the grain boundaries of the equiaxed grains. Grain boundaries, possessing higher interfacial energy, provide enhanced nucleation driving forces and faster atomic diffusion pathways. This promotes carbide precipitation at grain boundaries. With a heat treatment

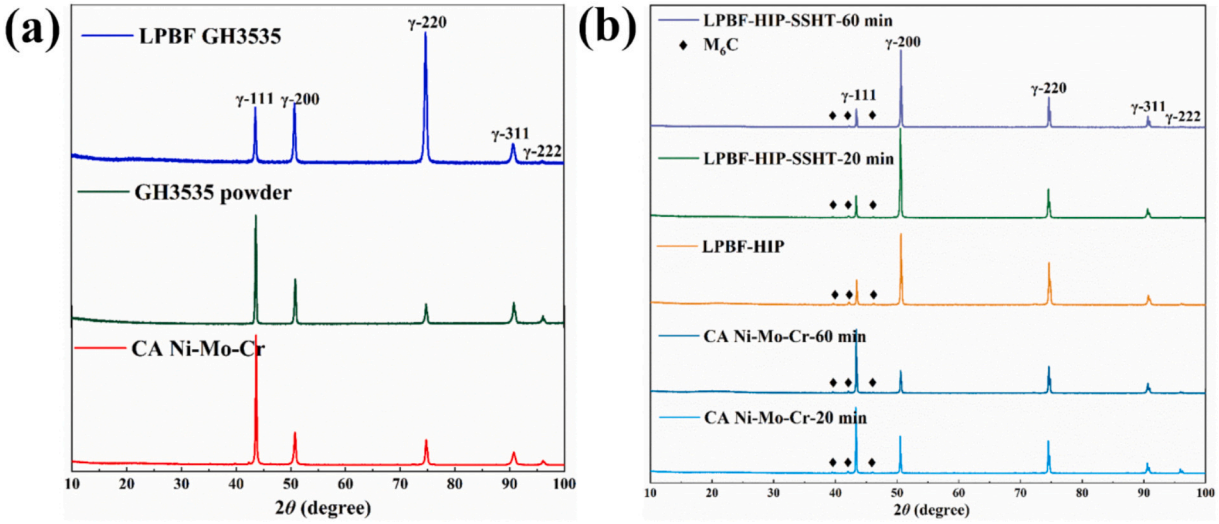

Fig. 2. XRD patterns of (a) pristine CA Ni-Mo-Cr, GH3535 powder, and LPBF GH3535 and (b) CA Ni-Mo-Cr GH3535 and LPBF GH3535 after heat treatment for different times.

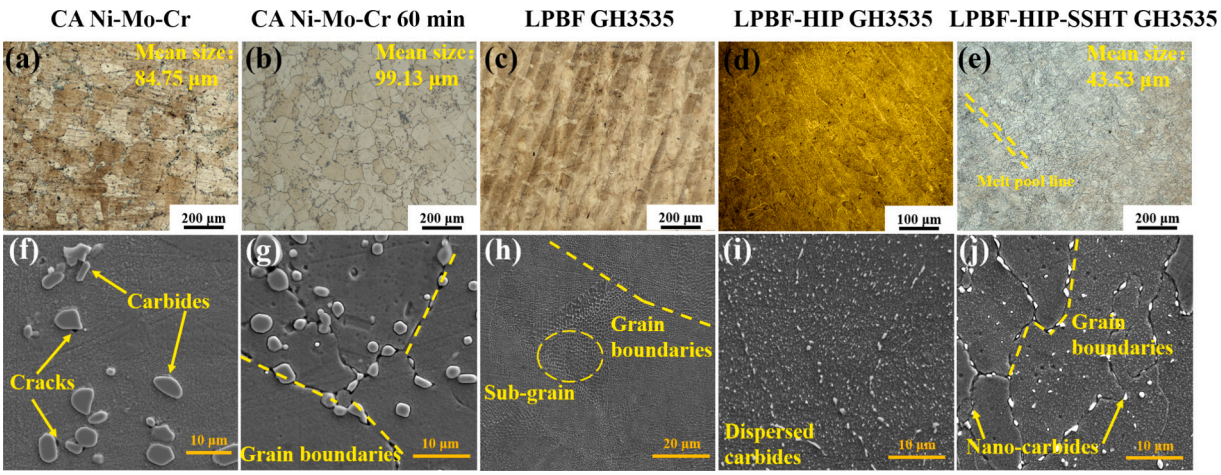

Fig. 3. Metallographic micrographs of (a) CA Ni-Mo-Cr, (b) CA Ni-Mo-Cr 60 min GH3535, (c) LPBF GH3535, (d) LPBF-HIP GH3535, and (e) LPBF-HIP-SSHT 60 min GH3535. The average size of the sample is counted and marked in the upper right corner of the figure. (f) to (j) present the corresponding SEM images for each sample.

duration of 60 min, more carbides precipitate at the grain boundaries. Fig. 3 (c) displays a unique cellular sub-grain structure in the LPBF GH3535 sample, with sub-grain sizes of approximately 500 nm and a mean melt pool width of around 88.03 μm. Compared to the CA Ni-Mo-Cr sample, the LPBF GH3535 sample shows only minimal carbide precipitation. Fig. 3 (d) and (i) reveal that after HIP at 1050 °C, the cellular sub-grain structure in the LPBF sample partially disappears, and finer, more uniformly dispersed carbides are observed in the LPBF-HIP sample. In the LPBF-HIP GH3535 samples, carbides along the grain boundaries are larger, while intragranular carbides are smaller, with an average size of approximately 260 nm. Micrographs taken after the two-step heat treatment are shown in Fig. 3 (e) and (j). Grains of varying sizes are distributed along both sides of the melt-pool line (indicated by the yellow dashed line in Fig. 3 (e)), with larger carbides found along the grain boundaries. Due to the high deformation energy at the melt-pool junction, fine grains easily form during the solution treatment process [33]. Generally, compared to 20 min of heat treatment, a duration of 60 min favors the continued growth of larger grains. However, in the LPBF-HIP-SSHT GH3535 samples, a competitive relationship exists between grain growth and carbide precipitation. Some smaller grains gradually merge and grew into larger grains, while the increased precipitation of carbides pins the grain boundaries, thus inhibiting the growth of larger grains. Further analysis of these carbides is required.

3.1.3. Carbides

As shown in Fig. 4(a), a high density of entangled dislocation lines was observed at the sub-grain boundaries in the LPBF samples. After HIP treatment, the sub-grain boundaries coarsened and partially disappeared, along with the unfolding or disappearance of the high-density dislocation lines (Fig. 4(b)). These results indicate that the matrix in the LPBF-HIP samples remains in the face-centered cubic γ phase. High-resolution imaging further revealed that the lattice constant was affected by the presence of carbides, with the lattice constant of the matrix in LPBF-HIP GH3535 measured at 0.2118 nm.

3.2. Mechanical properties

3.2.1. Impact performance

To assess the mechanical properties of GH3535 alloys, impact tests were conducted at room temperature and 200 °C on both CA Ni-Mo-Cr and LPBF GH3535, with the average impact energy values summarized in Table 4. At RT, the LPBF samples exhibited a significantly higher impact energy (116.54 J) compared to the CA Ni-Mo-Cr samples (15.29 J), with the difference spanning approximately one order of magnitude. The impact results at 200 °C show improved performance for both samples compared to RT, which is consistent with the typical behavior observed in most metallic alloys. Notably, the impact energy of LPBF GH3535 reached a peak of 214.9 J at 200 °C, surpassing the performance of traditional stainless steels and high-entropy alloys [34,35]. Fig. 5 illustrates the microstructural morphology of the impact fracture surfaces for both CA Ni-Mo-Cr and LPBF GH3535 alloys. As shown in

Table 4
Impact energy of CA Ni-Mo-Cr and LPBF GH3535 at RT and 200 °C.

Samples	Temperature	Impact energy (J)
CA Ni-Mo-Cr	RT	15.29
LPBF GH3535	RT	116.54
CA Ni-Mo-Cr	200 °C	101.55
LPBF GH3535	200 °C	214.9

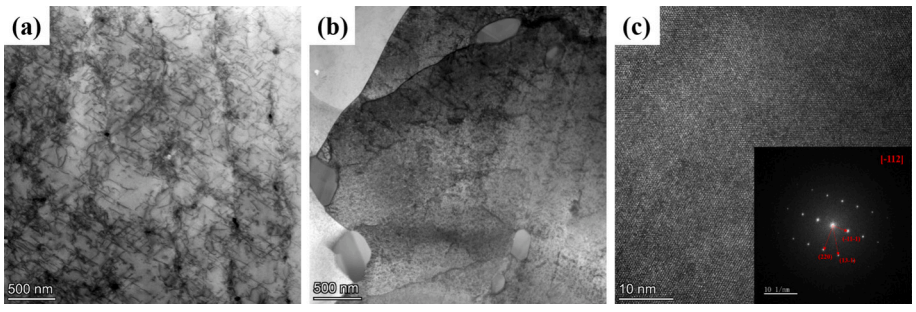

Fig. 4. TEM images of (a) LPBF GH3535 and (b) LPBF-HIP GH3535. (c) TEM HAADF and FFT patterns of LPBF-HIP GH3535.

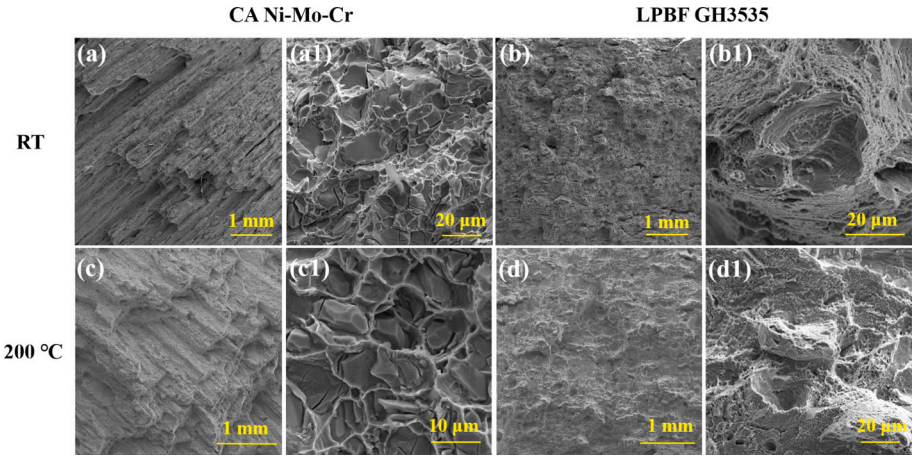

Fig. 5. Impact fracture surfaces of GH3535 alloys: (a) CA sample at RT, (b) LPBF sample at RT, (c) CA sample at 200 °C, and (d) LPBF sample at 200 °C. (a1)-(d1) are magnified views of (a)-(d), respectively.

Fig. 5 (a) and (c), the CA sample exhibited clearly visible fracture steps at low magnification. At higher magnification (Fig. 5(a1) and Fig. 5 (c1)), the fracture surface displayed a sugar-like granular appearance, indicative of intergranular fracture, which suggests relatively high brittleness for the CA sample.

In contrast, the fracture surfaces of the LPBF samples were characterized by a high density of dimples and tear ridges, which are indicative of good plasticity and ductile fracture behavior. Dimples are typically associated with deformation and energy absorption under stress, while tear ridges reflect localized stress concentration and rapid crack propagation during fracture. Fig. 5(b) and Fig. 5(d) show the macroscopic fracture morphology of the LPBF samples at RT and 200 °C. The fracture surfaces were rough, with numerous micro-pits. As shown in Fig. 5(b1) and Fig. 5(d1), the LPBF samples exhibited a notably higher density of dimples, indicating enhanced plastic deformation. The grain refinement effect due to the cellular sub-grain structure contributes to further improvements in impact toughness. Additionally, the stability of the cellular sub-grains (Fig. 5(b1)) increased the density of grain boundaries on the cross-section, further enhancing toughness.

3.2.2. *Tensile properties*

Fig. 6 presents the tensile engineering stress-strain curves of CA Ni-Mo-Cr, CA Ni-Mo-Cr-SSHT, LPBF-GH3535, and LPBF-HIP-SSHT GH3535 alloys at both RT and 700 °C. The LPBF GH3535 alloy demonstrates higher ultimate tensile strengths compared to the CA Ni-Mo-Cr alloy at both RT and 700 °C (Table 5). Under RT tensile testing conditions, the unheat-treated CA samples exhibit a high ultimate tensile strength of 1011.04 MPa. However, due to the cellular sub-grains and

Table 5
Tensile properties of GH3535 alloys at different temperatures.

Temperature	Samples	Ultimate tensile strength (MPa)	Yield strength (MPa)	Elongation (%)
RT	CA Ni-Mo-Cr	1011.04	859.02	7.13
	CA-20	487.94	332.54	8.10
	CA-60	552.64	294.72	16.30
	TM-40 [36]	817.31	310.84	60.98
	LPBF	958.78	633.73	30.20
	LPBF-HIP-SSHT-20	856.96	451.13	37.10
	LPBF-HIP-SSHT-60	861.60	382.06	39.60
	CA	718.29	655.31	12.60
	CA-20	523.40	205.0	52.5
	CA-60	542.55	208.0	52.3
	TM-40 [36]	455.98	196.57	28.7
700 °C	LPBF	573.37	500.37	18.2
	LPBF-HIP-SSHT-20	589.55	350.99	24.4
	LPBF-HIP-SSHT-60	616.02	363.73	27.0

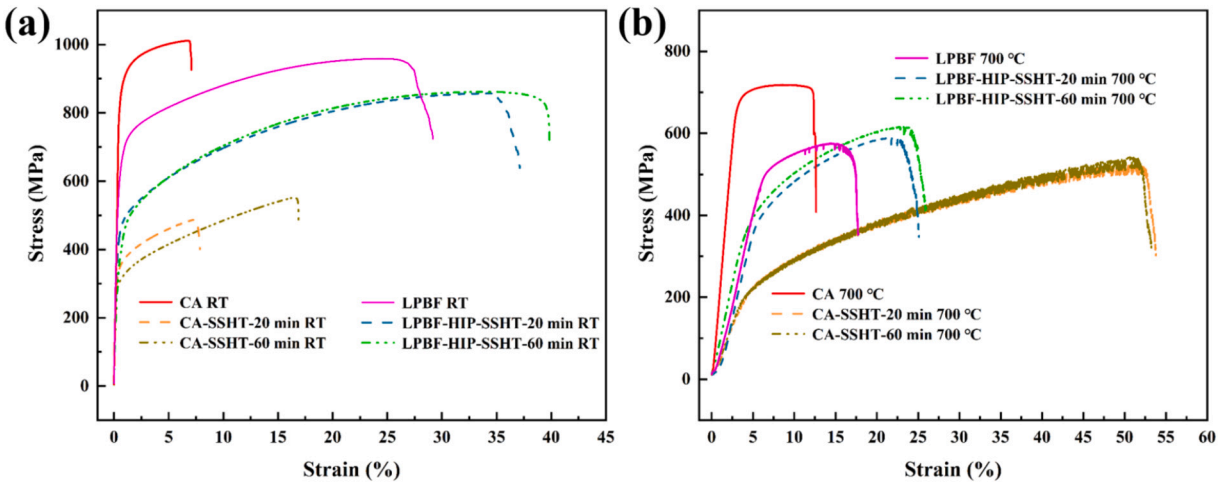

Fig. 6. Tensile engineering stress-strain curves of CA Ni-Mo-Cr and LPBF GH3535 alloys before and after heat treatment at RT (a) and 700 °C (b).

entangled dislocations introduced by LPBF GH3535, its ultimate tensile strength, yield strength, and elongation are superior to those of the CA-SSHT samples. After heat treatment, the ductility of both CA Ni-Mo-Cr and LPBF GH3535 improves due to carbide precipitation and microstructure changes. At 700 °C, the yield strength and ultimate tensile strength of both CA Ni-Mo-Cr and LPBF GH3535 alloys are significantly lower than those at RT. Specifically, the ultimate tensile strength of the LPBF-HIP-SSHT-60 min sample decreases to approximately 616.2 MPa, which remains higher than that of the CA-SSHT-60 min sample (542.55 MPa). However, the maximum elongation of the LPBF samples at 700 °C is approximately half of that of the CA-SSHT samples (~52.5 %). In comparison with the TM-40 sample, which was heat-treated at 1177 °C for 40 min in the previous study [36], the LPBF-HIP-SSHT sample in this work exhibits higher ultimate tensile strength and yield strength at both RT and 700 °C, although its elongation is lower than that of the TM-40. A typical hardening response is observed in the tensile true stress-strain curves for both alloys at RT, with a smooth curve. However, serration flow behavior is evident at 700 °C after yield, which is attributed to the deformation mechanism [37].

3.3. Irradiation effects

3.3.1. Phase structure after irradiation

The GIXRD patterns of the LPBF, LPBF-HIP, and LPBF-HIP-SSHT GH3535 samples, subjected to He^{2+} ion irradiation at fluences of 5×10^{16} and 5×10^{17} ions/cm^2 at 700 °C, are shown in Fig. 7. The XRD results clearly reveal that all irradiated samples exhibit three diffraction peaks corresponding to γ(111), γ(200), and γ(220), indicating that the FCC phase structure is preserved after irradiation. In addition to the main peaks, diffraction peaks corresponding to M_6C were also observed in the irradiated samples. Peaks attributed to $M_{23}C_6$ were observed at approximately $2\theta = 38°$, while peaks related to carbides containing Mo and Si appeared around $2\theta = 64.5°$. These observations are in agreement with those reported by other researchers. Previous studies have indicated that prolonged exposure to high temperatures (700 °C) can cause the transformation of some MC_2 carbides into MC_6 carbides [38]. This study further confirms that carbide precipitation became more pronounced after irradiation.

3.3.2. Irradiation-induced helium bubbles

Fig. 8 presents BF-TEM images of CA Ni-Mo-Cr, LPBF GH3535, LPBF-HIP GH3535, and LPBF-HIP-SSHT GH3535, illustrating the irradiation-induced damage region from He^{2+} ion irradiation, with an average depth of 1000 nm and fluences of 5×10^{16} and 5×10^{17} ions/cm^2. At the peak damage levels of 1.9 and 19 dpa, irradiation-induced defect structures were observed to evolve with varying doses. As shown in Fig. 8 (a), under high-temperature irradiation, the irradiated region of the CA Ni-Mo-Cr sample exhibits a uniformly "wrinkled" morphology, characterized by prominent dislocation lines ranging in size from 100 to 500 nm. Helium bubbles are dispersed between the dislocation lines. This "wrinkled" morphology is absent in the non-irradiated region. As the irradiation dose increased to 5×10^{17} ions/cm^2 (Fig. 8(e)), a significant reduction in dislocation lines was observed, leading to extensive helium bubble growth. In the peak irradiation region, stacking of helium bubbles was observed.

After low-dose irradiation of the LPBF samples at 700 °C (Fig. 8 (b)), the cellular sub-grain structure was partially lost, leaving numerous entangled dislocation lines. High-density helium bubbles were diffusely distributed along the remaining sub-grain boundaries, while the interior of the sub-grains exhibited relatively lower helium bubble density. This suggests that sub-grain boundaries act as effective sinks for helium bubbles, absorbing them and preventing their growth during high-temperature irradiation. However, at higher irradiation doses, as shown in Fig. 8 (f), extended high-temperature irradiation resulted in the disappearance of the sub-grain structure in the LPBF samples, with dislocation lines diffusely spread across the irradiated region. As the sub-grain boundaries disappeared, small helium bubbles initially located around the grain boundaries rapidly coalesced, growing into larger bubbles, leading to an increase in bubble size and a decrease in bubble number density.

Fig. 4 highlights that the HIP process resulted in the loss of most sub-grain boundaries, while the entangled dislocation lines straightened and disappeared. Under low-dose irradiation, residual sub-grain boundaries were still present (Fig. 8(c)), but the density of helium bubbles around these boundaries was lower than that around the carbides. The absorption and capture effects of the sub-grain boundaries on helium bubbles were weaker compared to those of M_6C, although no significant difference in bubble size was observed. The M6C interface, being a phase boundary with higher atomic mismatch and interfacial energy, exhibited a much higher binding energy for He atoms than conventional interfaces, as indicated by simulation results [39]. Fig. 8(g) shows the distribution of helium bubbles around the carbides in LPBF-HIP GH3535 under high-dose irradiation. Numerous nano-sized helium bubbles were observed within the carbide phase. These nano-sized bubbles were smaller and more densely packed compared to those at the same depth in the matrix. During He ion irradiation, helium bubbles that were absorbed at the M_6C/γ-Ni interface tended to recombine, thereby inhibiting their further diffusion and growth.

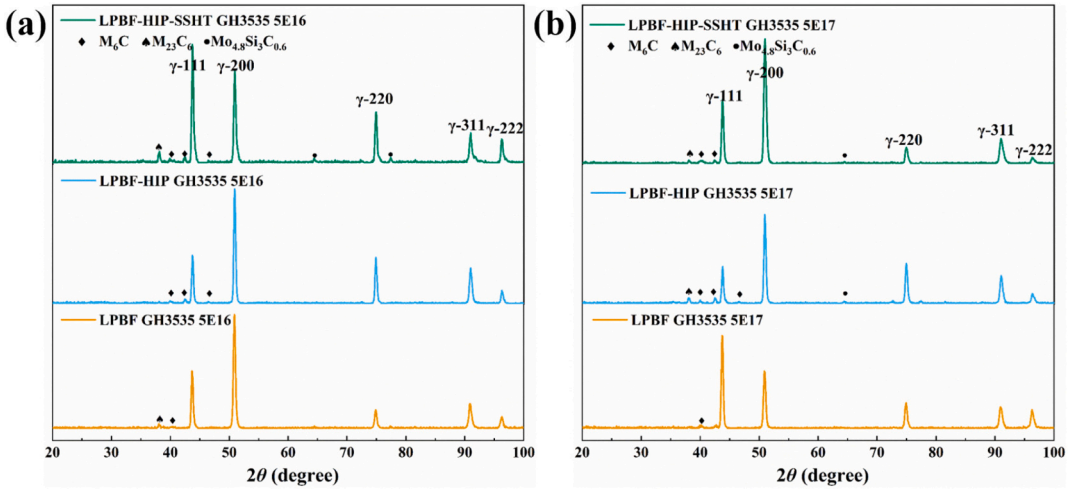

Fig. 7. GIXRD spectra obtained on three types of LPBF GH3535 alloy after irradiation at 700 °C with He^{2+} ion fluence of (a) 5×10^{16} and (b) 5×10^{17} ions/cm^2. Typical peaks characteristic of austenite are visible.

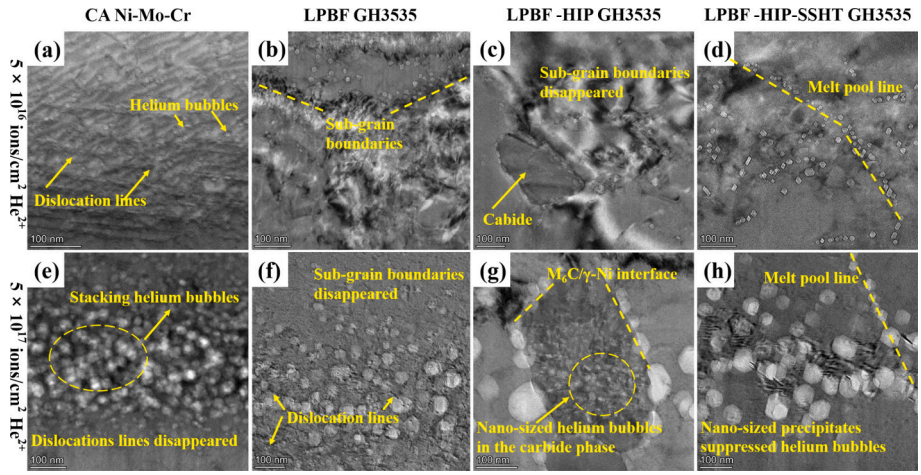

Fig. 8. TEM image of irradiated regions of (a) and (e) CA Ni-Mo-Cr samples, (b) and (f) LPBF GH3535 samples, (c) and (g) LPBF-HIP GH3535 samples, and (d) and (h) LPBF-HIP-SSHT GH3535 samples at 700 °C with the He^{2+} ion fluence of (a–d) 5×10^{16} and (e–f) 5×10^{17} ions/cm^2.

As shown in Fig. 8(d), the sub-grain structure at the M_6C/γ-Ni interface of the LPBF-HIP-SSHT samples was eliminated after low-dose irradiation, and dislocation lines disappeared, with no distinct grain boundaries observed. Following heat treatment, additional nano-sized precipitates (approximately 5 nm) formed, with these carbide precipitates regularly distributed along the melt pool. Helium bubbles were also diffusely distributed around the small nano-carbides. Fig. 8(h) indicates that the melt pool structure persisted even at high doses. The absorption effect of the melt pool on helium bubbles remained significant, with helium bubbles around the melt pool in the peak irradiation region measuring only 20 nm, while those at the same depth in other regions ranged from 40 to 70 nm. Thus, nano-sized precipitates dominated the size and distribution of helium bubbles in the LPBF-HIP-SSHT samples. Notably, at high doses, the helium bubbles in the peak-damage region exhibited faceted structures, which transitioned to spherical forms as the dose increased further.

The number density and mean size of the helium bubbles in the peak irradiation regions were measured, and the statistical results for the various samples are summarized in Table 6. After irradiation at 700 °C with a He^{2+} ion fluence of 5×10^{16} ions/cm^2, the mean size of the helium bubbles in the LPBF GH3535 specimen (12.82 nm) and the LPBF-HIP-SSHT GH3535 specimen (13.41 nm) were smaller than those in the LPBF-HIP GH3535 specimen (31.93 nm). In contrast, the number densities of the helium bubbles in the LPBF GH3535 specimen (3.11×10^{23} m^{-3}) and the LPBF-HIP-SSHT GH3535 specimen (3.56×10^{23} m^{-3}) were slightly higher than that in the LPBF-HIP specimen (0.93×10^{23} m^{-3}). Upon increasing the irradiation fluence to 5×10^{17} ions/cm^2, all three samples exhibited an increase in helium bubble size and a decrease in number density; However, the LPBF GH3535 and LPBF-HIP-SSHT GH3535 specimens showed relatively consistent helium bubble sizes and number densities.

Table 6
The number density and mean size of helium bubbles at different irradiated LPBF GH3535 samples.

Samples	700 °C 5×10^{16} ions/cm^2		700 °C 5×10^{17} ions/cm^2	
	Mean size (nm)	Number density (10^{23} m^{-3})	Mean size (nm)	Number density (10^{23} m^{-3})
LPBF	12.82 ± 3.47	3.11	39.84 ± 12.30	1.61
LPBF-HIP	31.93 ± 8.94	0.97	61.01 ± 24.65	0.58
LPBF-HIP-SSHT	13.41 ± 3.11	3.56	42.73 ± 10.26	1.62

3.3.3. Radiation-induced hardening

The radiation-induced hardening of different types of CA Ni-Mo-Cr and LPBF GH3535 samples was evaluated using a nanoindentation technique. Figs. 9(a)–(d) show the nanoindentation hardness (H) as a function of indentation depth (h) for both unirradiated and irradiated samples. The results indicate that the hardness of LPBF GH3535 is greater than that of CA Ni-Mo-Cr. To eliminate the effect of surface artifacts, data from depths less than 50 nm were discarded for all samples. As shown in Figs. 9(c) and (d), various heat treatments for LPBF GH3535 significantly affected the nano-hardness of the irradiated samples. The measured hardness for all samples decreased with increasing depth. This trend can be explained by the Nix–Gao model [40]. To further assess the irradiation-hardening effects in the studied alloys, the square of the nanoindentation hardness (H^2) and the reciprocal of the indentation depth (h^{-1}) were plotted, following the method proposed by Kasada et al. [41], as shown in Figs. 9 (e)–(h). For the irradiated alloys, a linear relationship between H^2 and h^{-1} can be observed in the region of h > 250 nm. In the H^2-h^{-1} profiles of the irradiated samples, different slopes were observed at various depth intervals. The variation in slope suggests that the hardness is influenced by both the irradiated layer and the substrate at different deformation stages. From the nanoindentation data in Table 7, the values of H_0 and ΔH_0, along with the irradiation-induced hardness increment ($\Delta H_0^{irr} = H_0^{irr} - H_0^{unirr}$), were summarized. It can be seen that the degree of hardening for the CA sample is higher than that for the LPBF samples after high-temperature irradiation. Notably, except for the LPBF-HIP-SSHT samples, all irradiated samples exhibited hardening behavior compared to the unirradiated samples. This anomalous trend may be attributed to microstructural changes in the matrix after heat treatment, such as the precipitation of carbides, the disappearance of cellular sub-grain boundaries, and the effect of helium bubbles. Overall, in terms of nano-hardness, the LPBF-HIP-SSHT sample exhibited greater stability before and after irradiation, which is beneficial for providing data to support the application of new structural materials.

4. Discussion

The heat treatment process is a crucial method for improving the properties of nickel-based superalloys, primarily affecting grain size and the precipitation of secondary phases. Collins [42] reported that the addition of elements such as Mo or Si, which promote the formation of M_6C carbides in Hastelloy N alloys, resulted in an increased carbide volume and a corresponding decrease in grain size. Mao et al. [43] conducted experiments at various temperatures and durations to determine the optimal solution treatment parameters for hot-rolled

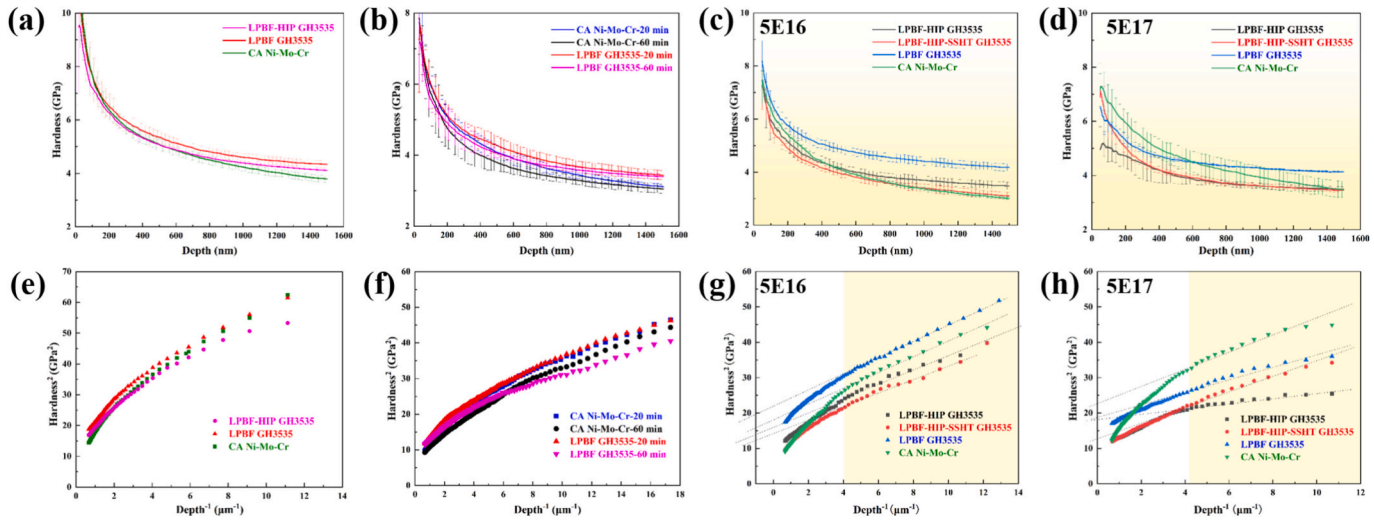

Fig. 9. Average nano-hardness measurements as a function of depth (distance from the irradiated surface) of all GH3535 samples at different conditions are shown in (a) and (b) before and after heat treatment, (c) and (d) ion irradiation at 700 °C with fluence of 5×10^{16} ions/cm^2 and 5×10^{17} ions/cm^2, and corresponding profiles of H^2 versus 1/h are shown in (e)–(h), respectively.

Table 7
Nano-hardness of samples before and after irradiation.

Samples	Unirradiated	700 °C 5 × 10^{16} ions/cm^2		700 °C 5 × 10^{17} ions/cm^2	
	H_0 (GPa)	H_0 (GPa)	ΔH_0^{irr} (GPa)	H_0 (GPa)	ΔH_0^{irr} (GPa)
CA	3.114	3.987	0.873	4.756	1.642
LPBF	3.873	4.427	0.554	4.32	0.447
LPBF-HIP	3.546	3.729	0.183	4.253	0.707
LPBF-HIP-SSHT	3.606	3.506	−0.1	3.562	−0.044

GH3536 alloy. They found that complete recrystallization occurred, with a uniform grain size distribution, when the temperature exceeded 1125 °C. Similarly, the CA-SSHT samples in this study also exhibited uniform equiaxed structures, indicating complete recrystallization. Zhang et al. [44] demonstrated that GH3535 alloy underwent recrystallization and grain growth, accompanied by partial dissolution of the primary M_6C carbides, after heat treatment at 1177 °C for 20 min. After heat treatment at 1177 °C for 60 min, the LPBF-HIP-SSHT samples showed a high density of uniformly distributed carbides. In comparison, the average grain size of the CA-SSHT samples was 99.13 μm, while the LPBF-HIP-SSHT samples had a grain size of 43.53 μm, representing a 54 % reduction. He et al. [45] used the powder metallurgy-hot isostatic pressing (PM-HIP) process to fabricate GH3535 alloy and observed that the forged samples tended to form carbide clusters or bands, while the PM-HIP samples exhibited uniformly distributed carbide particles. In the LPBF-HIP samples, carbides were uniformly precipitated both within the grains and along the grain boundaries, with slightly larger carbides observed at the grain boundaries. After heat treatment, the LPBF-HIP-SSHT samples showed different grain size distributions on either side of the melt pool, due to the high deformation energy, with finer, nano-sized carbides precipitating along the melt pool boundaries. Han et al. [46] found that $M_{12}C$ carbides formed in GH3535 alloy during thermal exposure for up to 1000 h, significantly inhibiting grain boundary sliding and crack initiation. However, prolonged exposure led to carbide coarsening, making them potential sources of grain boundary cracks, thus decreasing ductility. Upon analyzing the carbides in the LPBF GH3535 samples before and after heat treatment, it was found that only M_6C carbides were present. The LPBF-HIP-SSHT samples exhibited superior ductility compared to the LPBF samples at both RT and elevated temperatures. The dispersion of nano-sized carbides played a more significant role in enhancing the ductility of LPBF GH3535 than the cellular sub-grain boundaries.

With increasing irradiation dose, the size of helium bubbles in the GH3535 samples increased, while their number density decreased. Liu et al. [47] demonstrated that bubble migration and coalescence mechanisms dominated the coarsening of helium bubbles when the annealing temperature was below 800 °C. Generally, the introduction of interfaces can enhance the radiation resistance of materials. Previous studies have shown that the TiC/316 L interface effectively suppresses helium bubble migration [21]. An increased number of nano-grain interfaces can trap a significant amount of He atoms in GH3535 superalloys [48]. As shown in Fig. 10, the cellular sub-grains and entangled dislocation lines in the LPBF samples suppress helium bubble formation under high-temperature He^{2+} ion irradiation conditions. Similar results have been reported in studies on nickel alloys and stainless steel [6,23,49]. Likewise, in the LPBF-HIP-SSHT samples, a large number of uniformly

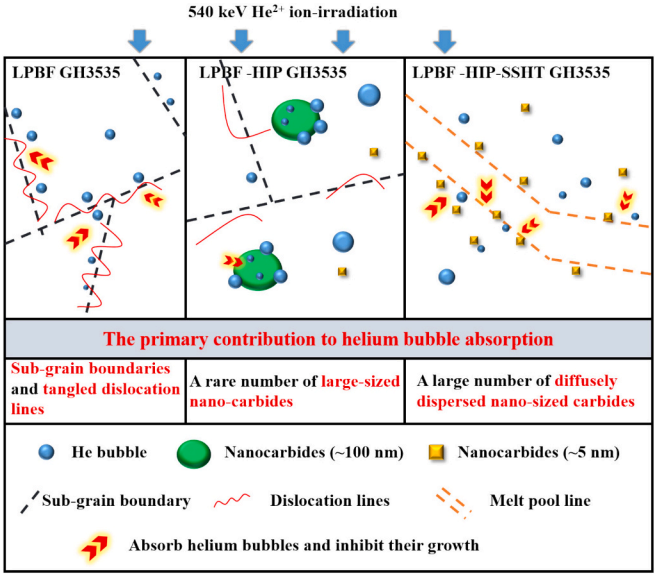

Fig. 10. Schematic illustration of bubble formation and growth in He-irradiated LPBF GH3535, LPBF-HIP GH3535, and LPBF-HIP-SSHT GH3535 samples.

dispersed nano-sized carbides precipitate along the melt pool, providing a sufficiently large number of carbides/γ-Ni interfaces to inhibit helium bubble migration and growth. Thus, the dispersion of a large quantity of nano-sized secondary carbides is more effective in improving irradiation resistance. The LPBF-HIP samples eliminated the residual stresses and defects of the LPBF samples but caused some cellular sub-grains to disappear, entangled dislocations to open up, and a small number of large-sized nano-carbides to precipitate. As a result, the LPBF-HIP samples exhibited a less pronounced inhibition of helium bubbles compared to the LPBF and LPBF-HIP-SSHT samples.

5. Conclusion

In this study, GH3535 samples were fabricated through selective laser melting (SLM) technology, achieving a molding density of 99.996 %. Two novel types of LPBF samples were produced via the HIP and HIP-SSHT processes. The factors affecting the mechanical properties and irradiation behavior of the GH3535 samples were analyzed. The main conclusions are as follows:

1) Compared to the LPBF samples, the LPBF-HIP-SSHT samples exhibited enhanced ductility and impact toughness at both RT and elevated temperatures. The yield and ultimate tensile strengths of the LPBF-HIP-SSHT samples were higher than those of the CA-SSHT samples, although their elongation at elevated temperatures was lower than that of the CA-SSHT samples.
2) The LPBF and LPBF-HIP-SSHT samples displayed similar helium bubble sizes and number densities. This was attributed to the presence of a high number of small-sized, diffuse nano-carbides, which promoted the formation of high-density interfaces that could absorb helium bubbles and prevent their growth. The LPBF-HIP sample, however, lost some of its cellular sub-grains and entangled dislocation structures, leading to a reduction in its irradiation resistance.
3) The LPBF-HIP-SSHT GH3535 samples did not exhibit a hardening phenomenon after irradiation, indicating that the two-step heat treatment significantly improved the irradiation resistance of the LPBF samples.

CRediT authorship contribution statement

Zhangjie Sun: Writing – original draft, Methodology, Investigation, Formal analysis. **Feida Chen:** Writing – review & editing, Validation, Methodology, Funding acquisition. **Jianjian Li:** Writing – review & editing, Validation, Resources. **Kun Yang:** Validation, Methodology. **Xiaobin Tang:** Writing – review & editing, Validation, Methodology.

Declaration of competing interest

The authors declare that they have no known competing financial interests or personal relationships that could have appeared to influence the work reported in this paper.

Acknowledgement

This work was supported by the Natural Science Foundation of Jiangsu Province (Grant No. BK20231450); Project supported by Jiangsu Planned Projects for Postdoctoral Research Funds (Grant No. 2021K222B); and Project supported by the Fundamental Research Funds for the Central Universities (Grant No. NS2023029). We thank to the 320-kV platform at the Institute of Modern Physics, CAS for the support of irradiation experiment. We acknowledge the TEM and SEM tests in the Center for Microscopy and Analysis at Nanjing University of Aeronautics and Astronautics.

Appendix A. Supplementary data

Supplementary data to this article can be found online at https://doi.org/10.1016/j.matchar.2025.115587.

Data availability

Data will be made available on request.

References

[1] A. Horvath, E. Rachlew, Nuclear power in the 21st century: challenges and possibilities, Ambio (2016), https://doi.org/10.1007/s13280-015-0732-y.
[2] K. Grandin, P. Jagers, S. Kullander, Nuclear energy, Ambio (2010), https://doi.org/10.1007/s13280-010-0061-0.
[3] GIF, GIF R&D Outlook for Generation IV Nuclear Energy Systems 2018 Update, Nuclear Energy. (2018).
[4] C. Fu, J. Li, J. Bai, Y. Li, Q. Chen, G. Lei, J. Lin, Z. Zhu, Y. Meng, Effect of helium bubbles on irradiation hardening of additive manufacturing 316L stainless steel under high temperature He ions irradiation, J. Nucl. Mater. (2021), https://doi.org/10.1016/j.jnucmat.2021.152948.
[5] M. Song, M. Wang, X. Lou, R.B. Rebak, G.S. Was, Radiation damage and irradiation-assisted stress corrosion cracking of additively manufactured 316L stainless steels, J. Nucl. Mater. (2019), https://doi.org/10.1016/j.jnucmat.2018.10.044.
[6] X. Sun, F. Chen, H. Huang, J. Lin, X. Tang, Effects of interfaces on the helium bubble formation and radiation hardening of an austenitic stainless steel achieved by additive manufacturing, Appl. Surf. Sci. (2019), https://doi.org/10.1016/j.apsusc.2018.10.268.
[7] Y. Yamashita, T. Murakami, R. Mihara, M. Okada, Y. Murakami, Defect analysis and fatigue design basis for Ni-based superalloy 718 manufactured by selective laser melting, Int. J. Fatigue (2018), https://doi.org/10.1016/j.ijfatigue.2018.08.002.
[8] L. Xiao, Z. Peng, X. Zhao, X. Tu, Z. Cai, Q. Zhong, S. Wang, H. Yu, Microstructure and mechanical properties of crack - free Ni - based GH3536 superalloy fabricated by laser solid forming, J. Alloys Compd. (2022), https://doi.org/10.1016/j.jallcom.2022.165950.
[9] I. Šulák, T. Babinský, A. Chlupová, A. Milovanović, L. Náhlík, Effect of building direction and heat treatment on mechanical properties of Inconel 939 prepared by additive manufacturing, J. Mech. Sci. Technol. (2023), https://doi.org/10.1007/s12206-022-2101-7.
[10] J. Serp, M. Allibert, O. Beneš, S. Delpech, O. Feynberg, V. Ghetta, D. Heuer, D. Holcomb, V. Ignatiev, J.L. Kloosterman, L. Luzzi, E. Merle-Lucotte, J. Uhlíř, R. Yoshioka, D. Zhimin, The molten salt reactor (MSR) in generation IV: overview and perspectives, Prog. Nucl. Energy (2014), https://doi.org/10.1016/j.pnucene.2014.02.014.
[11] H. Boussier, S. Delpech, V. Ghetta, D. Heuer, D. Holcomb, V. Ignatiev, E. Merle, J. Serp, The Molten Salt Reactor in Generation IV: Overview and Perspectives, in: GIF Symposium, 2012.
[12] J. Bai, J. Li, C. Fu, C. Ren, S. Chen, Y. Li, Z. Li, Q. Chen, Z. Zhu, J. Lin, Effect of helium bubbles on the irradiation hardening of GH3535 welded joints at 650°C, J. Nucl. Mater. (2021), https://doi.org/10.1016/j.jnucmat.2021.153241.
[13] Q. Liu, B. Leng, J. Qiu, H. Yin, J. Lin, Z. Tang, Effect of graphite particles in molten LiF-NaF-KF eutectic salt on corrosion behaviour of GH3535 alloy, Corros. Sci. (2020), https://doi.org/10.1016/j.corsci.2020.108581.
[14] C. Liu, X. Tang, L. Cheng, B. Leng, X. Li, X.X. Ye, H. Huang, The characterization of corrosion layers of GH3535 and Inconel 625 alloys in molten KNO3-NaNO3 salts at 500 °C, Corros. Sci. (2022), https://doi.org/10.1016/j.corsci.2022.110406.
[15] H. Huang, J. Gao, B. Radiguet, R. Liu, J. Li, G. Lei, Q. Huang, M. Liu, R. Xie, Microstructural evolution and hardening of GH3535 alloy under energetic Xe ion irradiation at room temperature and 650 °C, J. Nucl. Mater. (2018), https://doi.org/10.1016/j.jnucmat.2017.12.006.
[16] W. Ren, G. Muralidharan, D.F. Wilson, D.E. Holcomb, Considerations of alloy N for fluoride salt-cooled high-temperature reactor applications, in: American Society of Mechanical Engineers, Pressure Vessels and Piping Division (Publication) PVP, 2011, https://doi.org/10.1115/PVP2011-57029.
[17] C. Guo, G. Li, S. Li, X. Hu, H. Lu, X. Li, Z. Xu, Y. Chen, Q. Li, J. Lu, Q. Zhu, Additive manufacturing of Ni-based superalloys: residual stress, mechanisms of crack formation and strategies for crack inhibition, Nano Mater. Sci. (2023), https://doi.org/10.1016/j.nanoms.2022.08.001.
[18] Y. Mu, X. Zhang, Z. Chen, X. Sun, J. Liang, J. Li, Y. Zhou, Modeling of crack susceptibility of Ni-based superalloy for additive manufacturing via thermodynamic calculation and machine learning, Jinshu Xuebao/Acta Metall. Sin. (2023), https://doi.org/10.11900/0412.1961.2023.00050.
[19] H. Yu, J. Liang, Z. Bi, J. Li, W. Xu, Computational Design of Novel Ni Superalloys with low crack susceptibility for additive manufacturing, Metall. Mater. Trans. A Phys. Metall. Mater. Sci. (2022), https://doi.org/10.1007/s11661-022-06653-x.
[20] W.R. Martin, J.R. Weir, Postirradiation creep and stress rupture of Hastelloy N, Nucl. Appl. (1967), https://doi.org/10.13182/nt67-a27871.
[21] Z. Sun, Y. Xu, F. Chen, L. Shen, X. Tang, L. Sun, M. Fan, P. Huang, Effects of ion irradiation on microstructure of 316L stainless steel strengthened by disperse nano TiC through selective laser melting, Mater. Charact. (2021), https://doi.org/10.1016/j.matchar.2021.111420.

[22] Z. Zhu, H. Huang, S. Min, J. Hou, W. Ji, Characterization of microstructure and hardening of SLM nickel-based alloy irradiated by He ions, J. Nucl. Mater. (2022), https://doi.org/10.1016/j.jnucmat.2022.153794.
[23] S. Shen, Z. Sun, L. Hao, X. Liu, J. Zhang, K. Yang, P. Liu, X. Tang, E. Fu, The mechanisms of inhibition effects on bubble growth in He-irradiated 316L stainless steel fabricated by selective laser melting, Materials (2023), https://doi.org/10.3390/ma16113922.
[24] Z. Shang, C. Fan, S. Xue, J. Ding, J. Li, T. Voisin, Y.M. Wang, H. Wang, X. Zhang, Response of solidification cellular structures in additively manufactured 316 stainless steel to heavy ion irradiation: an in situ study, Mater. Res. Lett. (2019), https://doi.org/10.1080/21663831.2019.1604442.
[25] C. Fu, J. Li, J. Bai, Q. Lei, R. Liu, J. Lin, Evolution of helium bubbles in SLM 316L stainless steel irradiated with helium ions at different temperatures, J. Nucl. Mater. (2022), https://doi.org/10.1016/j.jnucmat.2022.153609.
[26] Z. Yuan, F. Chang, A. Chen, F. Li, R. Ma, J. Bai, J. Zheng, Microstructure and properties of SLM-Hastelloy X alloy after different hot isostatic pressing + heat treatment, Mater. Sci. Eng. A (2022), https://doi.org/10.1016/j.msea.2022.143714.
[27] S. Sun, Q. Teng, Y. Xie, T. Liu, R. Ma, J. Bai, C. Cai, Q. Wei, Two-step heat treatment for laser powder bed fusion of a nickel-based superalloy with simultaneously enhanced tensile strength and ductility, Addit. Manuf. (2021), https://doi.org/10.1016/j.addma.2021.102168.
[28] Z. Hao, C. Ge, X. Li, T. Tian, C. Jia, Effect of heat treatment on microstructure and mechanical properties of nickel-based powder metallurgy superalloy processed by selective laser melting, Jinshu Xuebao/Acta Metall. Sin. (2020), https://doi.org/10.11900/0412.1961.2019.00365.
[29] P.K. Gokuldoss, S. Kolla, J. Eckert, Additive manufacturing processes: selective laser melting, electron beam melting and binder jetting-selection guidelines, Materials (2017), https://doi.org/10.3390/ma10060672.
[30] S. Fanmin, C. Suiyuan, W. Mingwei, L. Jing, L. Changsheng, The structure and properties of Inconel 718 superalloy powder prepared by vacuum induction melting gas atomization for laser direct metal deposition, Mater Res Express (2019), https://doi.org/10.1088/2053-1591/aaf1d6.
[31] B. Podgornik, M. Šinko, M. Godec, Dependence of the wear resistance of additive-manufactured maraging steel on the build direction and heat treatment, Addit. Manuf. (2021), https://doi.org/10.1016/j.addma.2021.102123.
[32] Z.Z. Li, Q.L. Nai, S.H. Mo, B.S. Wang, M. Wang, J.X. Dong, Effect of heat treatment on the microstructure and properties of nickel-based superalloy thin-wall pipe for the fourth-generation nuclear reactor, Gongcheng Kexue Xuebao/Chin. J. Eng. (2018), https://doi.org/10.13374/j.issn2095-9389.2018.05.007.
[33] Z. Liu, D. Zhao, P. Wang, M. Yan, C. Yang, Z. Chen, J. Lu, Z. Lu, Additive manufacturing of metals: microstructure evolution and multistage control, J. Mater. Sci. Technol. (2022), https://doi.org/10.1016/j.jmst.2021.06.011.
[34] R. Kacar, M. Acarer, An investigation on the explosive cladding of 316L stainless steel-din-P355GH steel, J. Mater. Process. Technol. (2004), https://doi.org/10.1016/j.jmatprotec.2004.03.012.
[35] D. Li, C. Wu, L. Xie, Y. Zhang, P.K. Liaw, W. Wang, Improving tensile and impact properties of Fe50Mn30Co10Cr10 high entropy alloy via microstructural engineering, Intermetallics 170 (2024) 108314, https://doi.org/10.1016/j.intermet.2024.108314.
[36] F.F. Han, B.M. Zhou, H.F. Huang, B. Leng, Y.L. Lu, J.S. Dong, Z.J. Li, X.T. Zhou, The tensile behavior of GH3535 superalloy at elevated temperature, Mater. Chem. Phys. (2016), https://doi.org/10.1016/j.matchemphys.2016.07.001.
[37] P.G. McCormigk, A model for the Portevin-Le Chatelier effect in substitutional alloys, Acta Metall. (1972), https://doi.org/10.1016/0001-6160(72)90028-4.
[38] L. Jiang, W. Yinling, R. Hu, R. Liu, X.X. Ye, Z. Li, X. Zhou, Formation of nano-sized M2C carbides in Si-free GH3535 alloy, Sci. Rep. (2018), https://doi.org/10.1038/s41598-018-26426-0.
[39] X.Y. Li, Y.G. Zhang, Y.C. Xu, X.B. Wu, X.S. Kong, X.P. Wang, Q.F. Fang, C.S. Liu, Interaction of radiation-induced defects with tungsten grain boundaries at across scales: a short review, Tungsten (2020), https://doi.org/10.1007/s42864-020-00039-5.
[40] W.D. Nix, H. Gao, Indentation size effects in crystalline materials: a law for strain gradient plasticity, J. Mech. Phys. Solids (1998), https://doi.org/10.1016/S0022-5096(97)00086-0.
[41] R. Kasada, Y. Takayama, K. Yabuuchi, A. Kimura, A new approach to evaluate irradiation hardening of ion-irradiated ferritic alloys by nano-indentation techniques, Fusion Eng. Des. (2011), https://doi.org/10.1016/j.fusengdes.2011.03.073.
[42] T.W. Cowan, Structural stability in superalloys, JOM (1968), https://doi.org/10.1007/bf03378756.
[43] Y. Mao, Y. Zhao, L. Liu, S. Ji, Z. Zhang, W. Niu, Z. Zhao, Z. Tian, Effect of solution heat treatment on microstructure and properties of GH3536 Superalloy BT - proceedings of the 12th international conference on advanced materials and engineering materials, in: L. Zhang (Ed.), Springer Nature Singapore, Singapore, 2024, pp. 531–543.
[44] W. Zhang, Z. Xu, L. Jiang, Effect of solution heat treatment on microstructure and properties of GH3535 superalloy, Xiyou Jinshu Cailiao Yu Gongcheng/Rare Met. Mater. Eng. 45 (06) (2016) 1583–1587, cnki:sun:cose.0.2016-06-034.
[45] Z. He, Y. Jiang, L. Chang, H. Huang, Helium ion irradiation-induced damage of powder metallurgy-hot isostatic pressed Ni-based alloy GH3535 for molten salt reactor applications, J. Nucl. Mater. (2024), https://doi.org/10.1016/j.jnucmat.2023.154871.
[46] F.F. Han, B.M. Zhou, H.F. Huang, B. Leng, Y.L. Lu, Z.J. Li, X.T. Zhou, Effect of long-term thermal exposure on the hot ductility behavior of GH3535 alloy, Mater. Sci. Eng. A (2016), https://doi.org/10.1016/j.msea.2016.07.034.
[47] J. Liu, H. Huang, A. Liu, Y. Li, The effects of post-irradiation isochronous annealing on defects evolution and hardening in Hastelloy N alloy, J. Nucl. Mater. (2021), https://doi.org/10.1016/j.jnucmat.2021.152855.
[48] Z. Zhu, H. Huang, O. Muránsky, J. Liu, Z. Zhu, Y. Huang, On the irradiation tolerance of nano-grained Ni–Mo–Cr alloy: 1 MeV He+ irradiation experiment, J. Nucl. Mater. (2021), https://doi.org/10.1016/j.jnucmat.2020.152694.
[49] J. Lin, F. Chen, X. Tang, J. Liu, S. Shen, G. Ge, Radiation-induced swelling and hardening of 316L stainless steel fabricated by selected laser melting, Vacuum (2020), https://doi.org/10.1016/j.vacuum.2020.109183.